Time Response of Two-Dimensional Gas-Based Vertical Field Metal–Semiconductor–Metal Photodetectors

Xia Zhao, Marc Currie, Adriano Cola, Fabio Quaranta, Eric Gallo, Jonathan E. Spanier, and Bahram Nabet

***Abstract*—We have fabricated and characterized 2-D gas-based, including 2-D electron gas (2DEG) and 2-D hole gas (2DHG), heterostructure metal–semiconductor–metal (MSM) photodetectors on GaAs. Both the high-speed measurement of time response and the simulation results show that a vertical field developed in the active absorption region due to the δ-doping layer facilitates one type of photogenerated carrier transport. In addition, the confined carriers facilitate collection of the optically generated carriers that reach them. The vertical field in the MSM structure that is created by a 2-D gas transforms a traditional lateral MSM device to a vertical one, although remaining as a planar structure, thus allowing a device design for high-speed performance without sacrificing the external quantum efficiency.**

***Index Terms*—Metal–semiconductor–metal (MSM), photodetector (PD), time response, 2-D electron gas (2DEG), 2-D hole gas (2DHG).**

I. Introduction

Metal–semiconductor–metal (MSM) photodetectors (PDs) [1] have been widely applied in optical communication systems for long- and short-haul transmissions [2], [3], high-speed optoelectronic integrated circuit connection, and high-speed sampling. The development of optical fiber transmission systems has greatly increased the demand for high-performance PDs. The advantages of the MSM structure PDs in applications are due to their planar process technology, which may be accomplished with as little as one photolithography step and allows their monolithic integration with other optical and electronic circuits [3]. Great effort has been made toward improving the bandwidth–efficiency product performance [4] as one of the major figures-of-merit for PDs employed in communication systems. The edge-coupled PDs, such as waveguide coupled, traveling wave [5]–[8], and unitraveling carrier [9], were developed to enhance the bandwidth–efficiency product by separating the optimizations of speed and internal quantum efficiency, and they have demonstrated impressive performance. However, they still suffer from low external quantum efficiency due to the difficulty in coupling of the optical beam to the thin absorption region. Vertically illuminated PDs are well recognized for their high quantum efficiency due to the efficient coupling between optical radiation and the active region. For MSM structures, the external quantum efficiency is mainly determined by the coverage percentage of the interdigitated fingers. In addition, reduction of distance between fingers to increase the speed of response has a concomitant increase in capacitance, necessitating a small detector area and, hence, reduction in the external quantum efficiency. On the other hand, the speed of MSM PDs cannot further be improved by shrinking the finger separations since the 2-D distribution of the electric field in the active region is such that carriers will transit in low-field regions below their saturated drift velocity [10]. The proposed devices remain planar, monolithically compatible with a high electron mobility transistor (HEMT) process, with high efficiency and high speed.

To take advantage of the vertically illuminated MSM structure, we have developed 2-D gas-based PDs, which transform the laterally developed internal field in the absorption region to a vertically oriented one. In these designs, the previously finger-separation-dependent transit time is then determined by the much smaller thickness of the absorption region; hence, the speed of the PD can be enhanced by optimizing the thickness of the absorption region rather than by shrinking the separations of interdigitated fingers. Thus, high-speed performance can be achieved without sacrificing the external quantum efficiency in MSM structures. An important aspect of the operation of these devices is that the vertical transit of the optically generated carriers culminates in their collection in a reservoir of confined charge that is in quasi-equilibrium with metal (Schottky) contacts, thus circumventing the need for drift transit to the contacts. To further improve the internal quantum efficiency of these vertically illuminated PDs, we employ a resonant-cavity-enhanced structure [11].

Here, we report on fabricated 2-D electron gas (2DEG) [12] and 2-D hole gas (2DHG)-based MSM PDs. Emphasis is on their time response that is relatively independent of the finger separation for 2DEG, whereas the tail of response is

Manuscript received September 18, 2007; revised February 20, 2008. This work was supported in part by the National Science Foundation (NSF) under Grants ECCS 0621811 and ECCS 0702716 and in part by the U.S. Army Research Office under Award W911NF-04-100308. The work of B. Nabet was supported by the NSF under Awards ECCS 0621811 and ECCS 0702716. The work of J. E. Spanier was supported by the U.S. Army Research Office under Award W911NF-04-100308 and NSF Award ECCS 0702716. The review of this paper was arranged by Editor C. Nguyen.

X. Zhao was with the Department of Electrical and Computer Engineering, Drexel University, Philadelphia, PA 19104 USA. She is now with Mosel Vitelic Corporation, San Jose, CA 95134 USA.

M. Currie is with the Naval Research Laboratory, Washington, DC 20375 USA.

A. Cola and F. Quaranta are with the Institute of Microelectronics and Microsystems, National Council of Research (IMM-CNR), 73100 Lecce, Italy.

E. Gallo, J. E. Spanier, and B. Nabet are with the Department of Electrical and Computer Engineering, Drexel University, Philadelphia, PA 19104 USA (e-mail: nabet@ece.drexel.edu).

Color versions of one or more of the figures in this paper are available online at http://ieeexplore.ieee.org.

Digital Object Identifier 10.1109/TED.2008.925242

0018-9383/$25.00 © 2008 IEEE

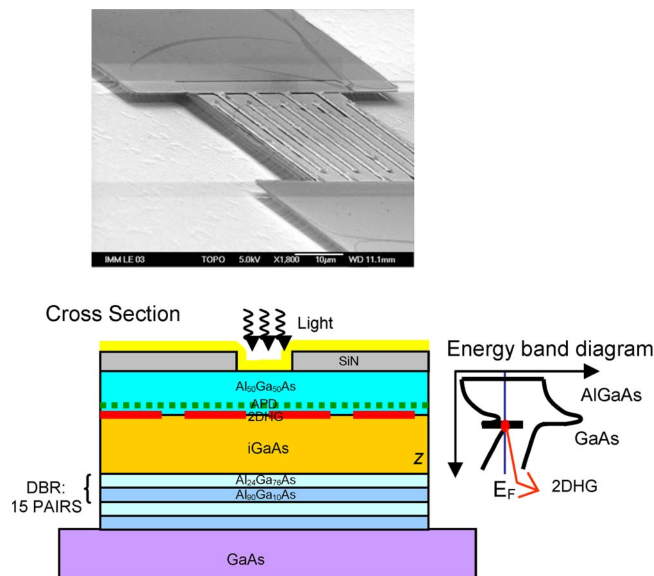

Fig. 1. Bottom: Cross section of the 2DHG device and a sketch of its energy band diagram. Top: Image of the fabricated device.

considerably shortened in 2DHG devices. Simulation of electrostatic landscape and transport within the absorption region is performed using Ramo's theorem, verifying a shortened transit path of the optically generated carriers and subsequent collection in a reservoir of 2-D charge.

II. Device Design and Fabrication

The devices consist of two Schottky contacts on top of a δ-layer modulation-doped AlGaAs/GaAs heterostructure. The wafers for device fabrication were grown by molecular beam epitaxy on a (100)-oriented semiinsulating GaAs substrate for 850-nm wavelength detection. Delta-doping layers of Si and Be for 2DEG and 2DHG, respectively, were employed. A sketch of the layered structure of the 2DHG device and its energy band diagram are shown in Fig. 1. The top shows the side view of the mesa-isolated fabricated device; interdigitated fingers are on AlGaAs and are deposited through a window etched into a Si_3N_4 passivation layer that remains between the contact pads and AlGaAs.

The layer structure consists of 15 pairs of quarter-wave $Al_{0.24}Ga_{0.76}As/Al_{0.9}Ga_{0.1}As$ distributed Bragg reflector with thicknesses of 67.6 and 59.6 nm, respectively, grown on a GaAs buffer layer. An intrinsic active GaAs absorption region of 117.5 nm was grown, which is designed to form a resonant cavity to improve the internal quantum efficiency, hence the responsivity of devices for wavelengths of interest. An intrinsic $Al_{0.3}Ga_{0.7}As$ layer covers the active absorption region for the 2DEG device and the same material with an Al component of 0.5, which provides the valence band offset of 0.21 eV [13], and is used for the 2DHG device to achieve better confinement of hole gas. This layer also enhances the Schottky barrier height and reduces surface recombination. We term this an "undoped" device. We also produce a δ-doped structure by adding an additional highly Si-doped thin atomic planar doping layer, namely, a δ-modulation-doping layer into the $Al_{0.3}Ga_{0.7}As$ layer with a 5-nm spacer layer away from the AlGaAs/GaAs junction for the 2DEG device. A Be-doped δ-modulation layer with a 7-nm spacer is used in the 2DHG device.

Device fabrication followed standard processes, including optical lithography, metal evaporation, liftoff, and mesa etching to obtain device isolation. Si_3N_4 (200-nm) was deposited for active area restriction planarization. The interdigitated electrodes were deposited with a Ti/Pt/Au multilayer, forming Schottky contacts to the semiconductor. The device active area is $40 \times 40\ \mu m^2$.

III. Simulation Results of Static and Dynamic Behaviors

A. Static Behavior

Device electrical properties were simulated with commercially available Integrated Systems Engineering (ISE) technology computer-aided design software, specifically the device simulator DESSIS. This software is based on a self-consistent solution of the Poisson's equation, the electron/hole continuity equations, and the energy conservation equations for electrons, holes, and lattice.

We simulated the 2DEG device with one unit cell due to the repetition of the interdigitated finger patterns and applied a reflective boundary condition for that unit cell. The simulation employs geometry with a finger width of 2 μm and a finger gap of 2 μm (W2G2), and the thickness of the active region is 1 μm. The Schottky barrier height is 0.7 V; thus, the contact potential is $V_{\rm sc} = -0.7$ V at the cathode, and $V_{\rm sa} = V_a - 0.7$ V at the anode, where V_a is the external applied bias. The δ-doped AlGaAs/GaAs heterostructure MSM (HMSM) PD was simulated. For the purpose of comparison, the undoped structure has also been simulated under the same condition.

Simulation results for the conduction band and carrier density, as shown in Fig. 2, and the electric field, as shown in Fig. 3, in doped and undoped devices are compared for a 5-V applied bias. The inset coordinates give x-direction along the length of the device, and y-direction along the depth.

In the undoped structure, although the carrier concentration at the interface is higher than that in the bulk, the electrons are not well confined, since AlGaAs and GaAs layers are both undoped, and carrier transfer is only due to the difference in electron affinity. In contrast, in the doped structure, a large carrier density reaching 10^{12} cm^{-2} is observed as is typical in modulation-doped field-effect transistor structures. The 2DEG is well confined within a distance of about 100 Å.

The corresponding 3-D views of the conduction bands are shown in Fig. 2 (left) for the undoped and δ-doped structures at a 5-V bias. We observe that the potential drop along the x-direction is steplike in the δ-doped structure, rather than a uniform downward slope from the cathode to the anode in the undoped structure. The MSM structure with Schottky contacts is essentially two diodes with a back-to-back configuration. A large fraction of the applied bias is expected to drop across the reverse-biased junction, and the rest across the forward-biased junction, before the critical point of flat band is reached [14]. As the bias voltage of 5 V is applied on the undoped structure, the reverse-biased depletion region extends to the anode. However, for the δ-doped structure, a

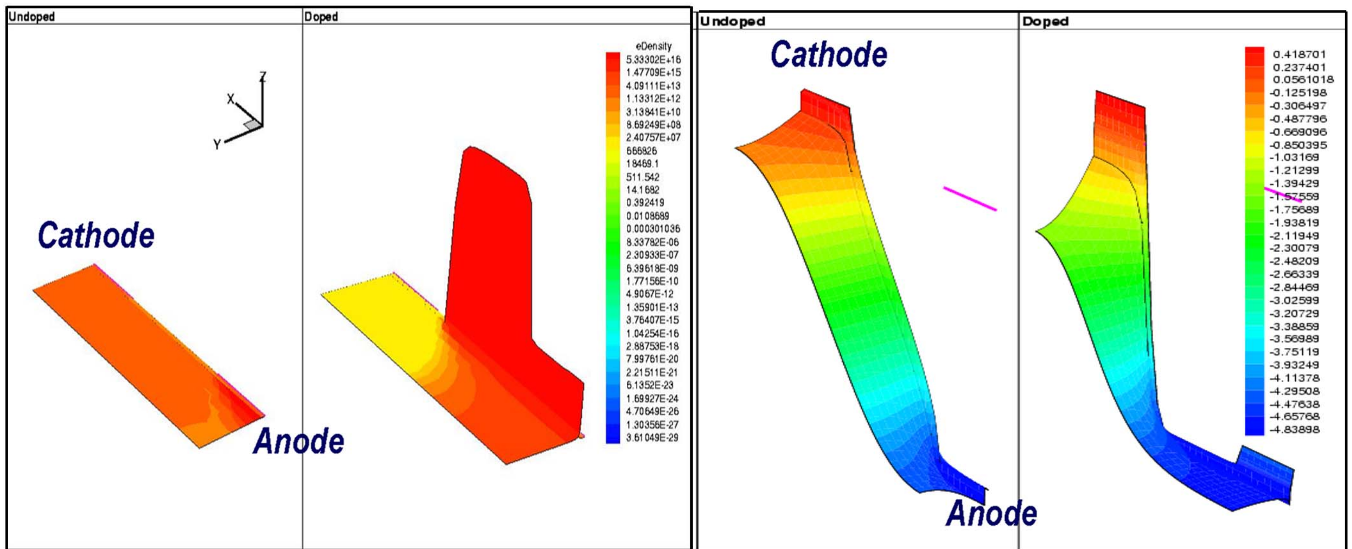

Fig. 2. Three-dimensional view of the electron concentration for the undoped (left) and δ-doped (second from left) HMSM PDs. Conduction band for the δ-doped (right) and undoped HMSM PDs (second from right).

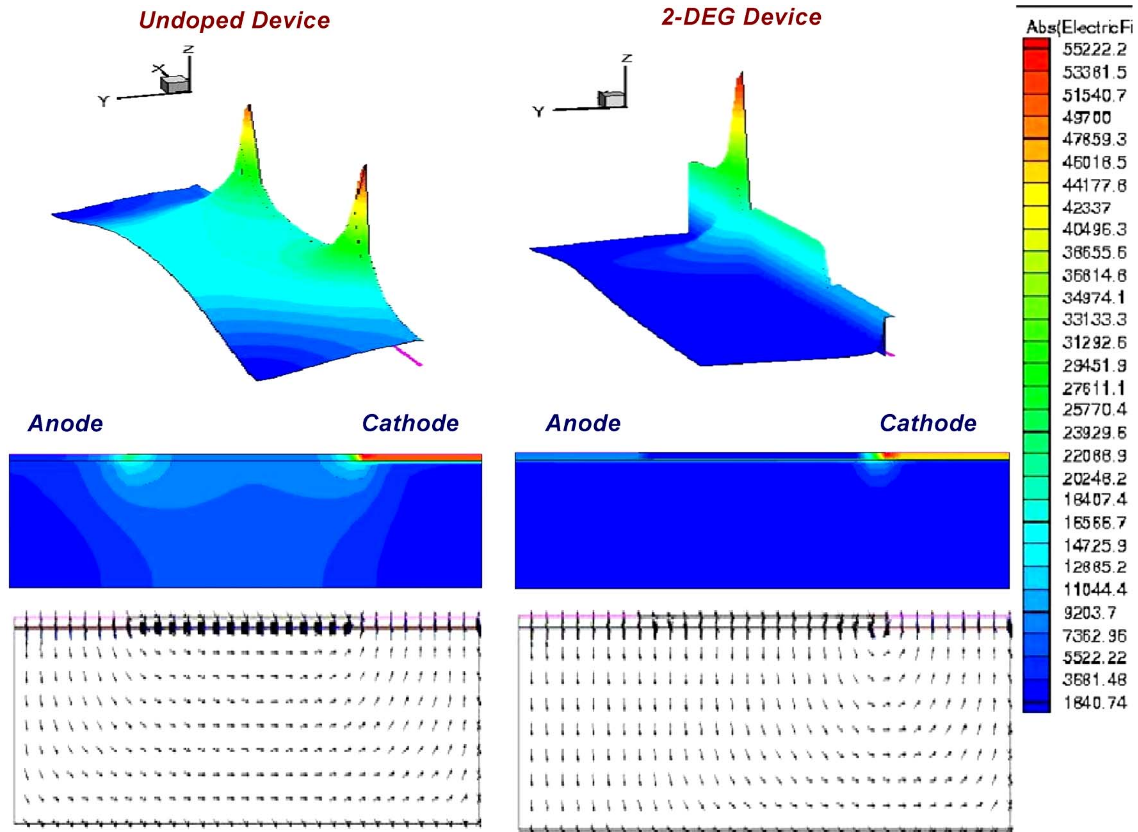

Fig. 3. Comparison of the electric field in the undoped (left) and delta-doped (right) devices. Top: 3-D view. Middle: 2-D cut. Bottom: Vector field.

highly concentrated 2DEG along the entire interface effectively screens the depletion of charges. In the 2-D case, the depletion length is given as $d_{2d} = 2\varepsilon(V_{\rm bi} + V_a)/qn_s$ [15], where d_{2d} is the width of depletion, $V_{\rm bi}$ is the built-in potential of the junction, V_a is the applied bias, and n_s is the 2-D carrier density. A rough estimation of the 2DEG concentration of $2.5 \times 10^{12}/\mathrm{cm}^2$, provided that the δ-doping level is $5 \times 10^{12}/\mathrm{cm}^2$, gives a depletion width of 0.057 μm at $V = 1$ V. For the 3-D case, the relationship of the depletion width with the doping level is given as $d_{3d} = \sqrt{2\varepsilon(V_{\rm bi} + V_a)/qn_v}$, where n_v is the 3-D carrier density. Given a background unintentional doping level of around $10^{15}/\mathrm{cm}^3$, the width of depletion is around 1.57 μm at $V = 1$ V. The extension of the depletion region in the 3-D absorption region is much wider than that in the 2DEG given the same applied voltage. The potential shows an abrupt drop in lateral directions, as shown in Fig. 2, and the depletion region, therefore, vertically extends. In other words, most of the region extending from the anode to the cathode

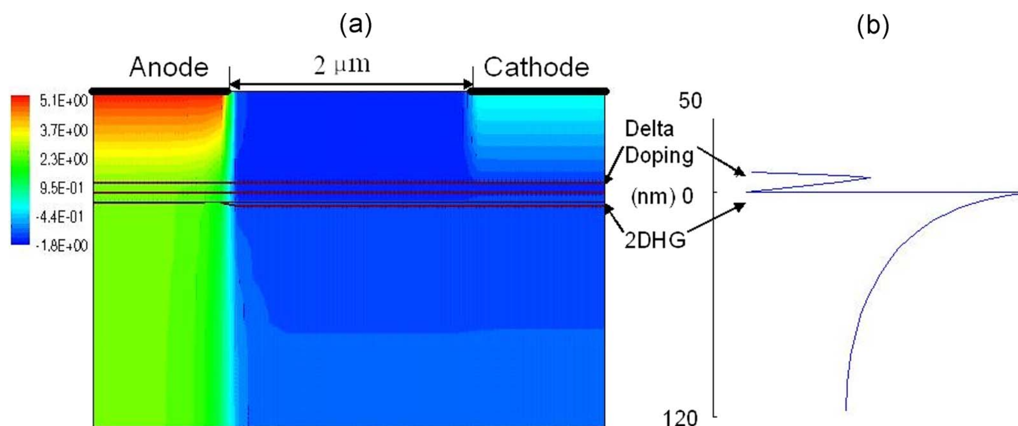

Fig. 4. Left: Simulation of the electrostatic potential in a 2DHG device. Right: Charge distribution calculated in a cross-sectional midpoint between the cathode and the anode.

remains under quasi-equilibrium, as screened by the 2-D gas from perturbation caused by the applied bias to cathode. This is verified by the fact that, experimentally, currents in tens of picoamperes were measured on this device, whereas changing the contacts to ohmic and retaining the same structure and device characteristics allow nine orders of magnitude more current to flow.

The corresponding electric field characteristics are shown in Fig. 3. It is observed that in the undoped device, the electric field is more symmetrically distributed, due to uniform potential drop between the anode and the cathode, whereas the electric field is concentrated in the vicinity of the cathode in the doped device. The field vector is horizontally oriented in the undoped structure in the bulk of the active region. In contrast, the δ-doped device presents a relatively vertically oriented field, which gradually changes to a lateral field when approaching the bottom of the active region. Following the electric field, electrons travel upward to the 2DEG in the doped device rather than move laterally first and then upward to the contacts in the undoped device. The vertical transit distance in the absorption region is about 20 times less than the distance between contacts.

Once the optically generated electrons reach the 2DEG, charge transport is greatly facilitated by the fact that it is a majority carrier effect subject to time constants of the order dielectric relaxation time, which is much shorter than the momentum relaxation time that governs drift velocity. That is, this sheet of carriers can effectively be treated as a quasi-equipotential conductor. It should be mentioned that the same electric field forces the holes deeper into the device; hence, the tail of response is adversely affected.

The static electrical properties for the 2DHG structure are similar, as shown in Fig. 4. Again, the 2DHG screens the effect of the potential applied to the anode, and the cathode remains in quasi-equilibrium with the 2DHG reservoir, i.e., the band bending and carrier distribution remain the same as in equilibrium. The major difference is that the vertical field developed is toward the 2DHG, which facilitates the hole transport and extends the electron transit path. The charge distribution midway between the cathode and the anode shows un-ionized dopants in the δ-doping layer, as well as hole distribution that leaks into the bulk. This is expected since the valence band discontinuity, which we deduced from reported experimental results, is low compared to the conduction band.

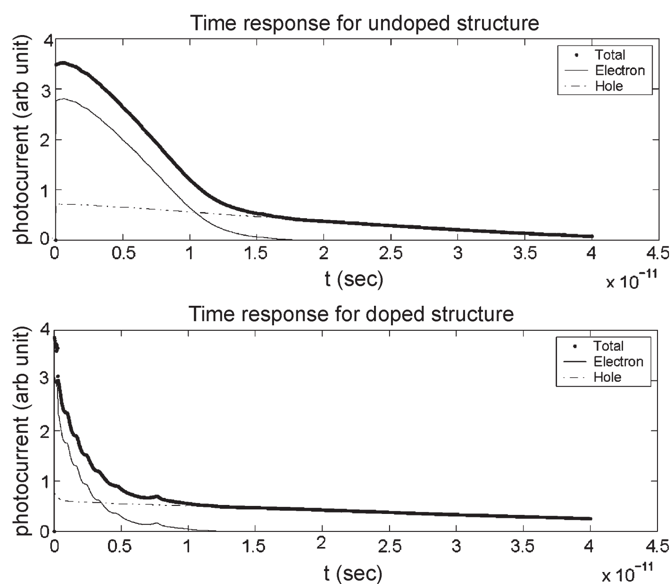

Fig. 5. Time-response comparison between the doped (bottom) and undoped (top) devices with separated contributions from electrons and holes.

B. Dynamic Behavior

The potential and electric field distributions previously calculated in this paper were used in modeling the dynamic behavior of the device using Ramo's theorem [16]. Several simulation methods have been employed to study the time response of PDs, including ensemble Monte Carlo (EMC) [10], [17], quantum–mechanical [18], and Ramo's [19]. EMC provides an exact numerical solution to the Boltzmann transport equation and is a complete analysis of transient carrier motions. It is particularly accurate and useful for cases such as nonequilibrium dynamics, where the carrier–carrier scattering events have to be incorporated. It has been shown that the PDs require a quantum–mechanical treatment using numerical solutions of the time-dependent Schrödinger equation as the dimension of the structure under investigation goes below 100 nm. In our case, the dimension under investigation of the absorption region is around 4 μm in length and about 118 nm in depth; hence, inclusion of quantum effects is not essential. Compared to EMC, Ramo's theorem is much less computationally intensive,

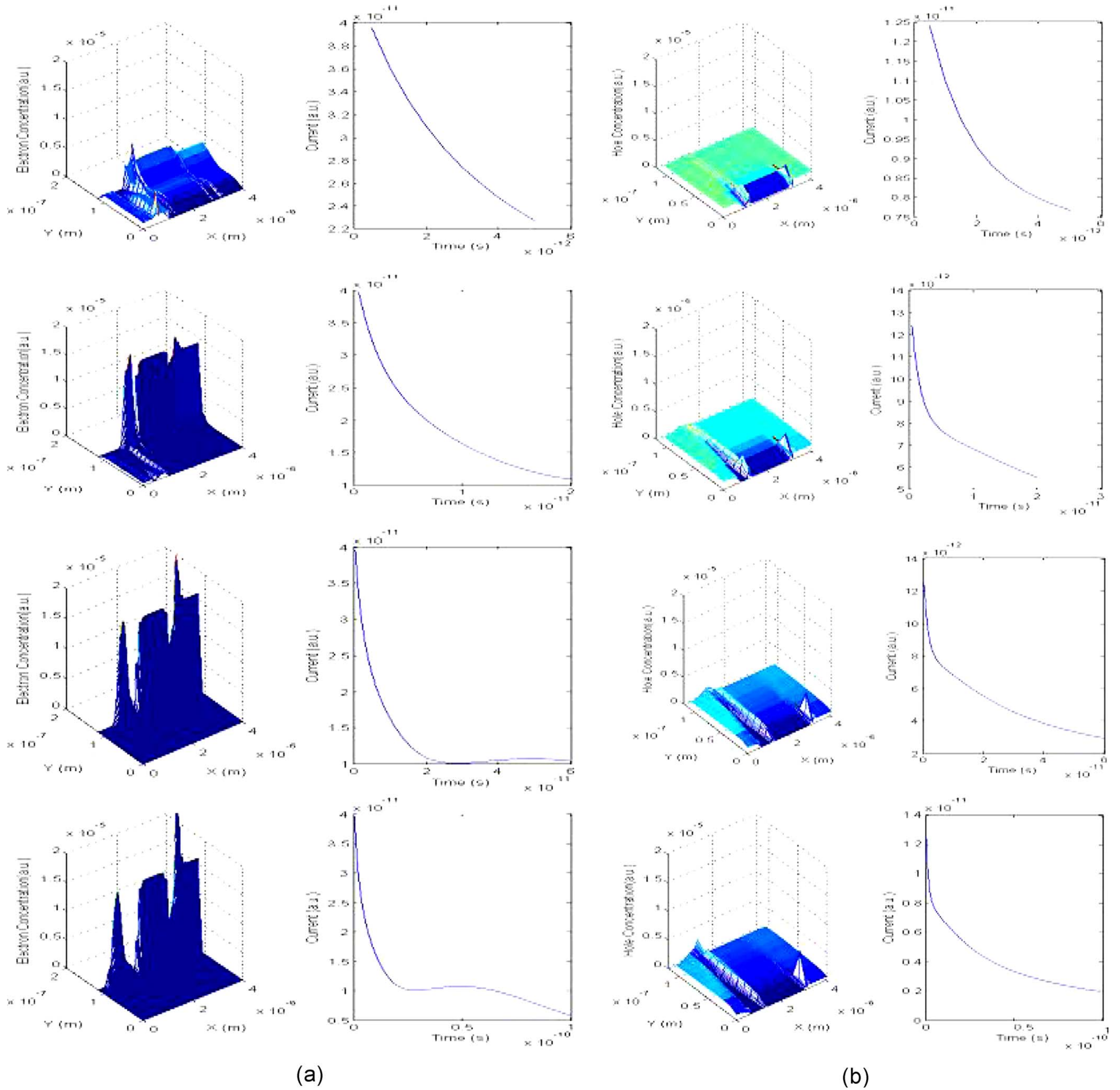

Fig. 6. Evolution of (a) electron and (b) hole concentrations and their corresponding contributions to the photocurrent.

whereas it retains the important physical characteristics of the device most notably in calculation of the current that is induced in the external circuitry while carriers move inside the device and have not yet reached the contacts.

Ramo's theorem was proposed in 1930s [16]. Its 1-D application for current calculation is introduced in [20], and the 2-D model was developed as [19]

$$J_{\mathrm{ph}} = \sum_{q} q\vec{v}(\vec{r})\frac{\vec{E}(\vec{r})}{V} \tag{1}$$

where J_{ph} denotes the induced density of current in the external circuit, E is the electric field, $v(r)$ is the velocity of a moving carrier, and V is the applied bias. The total induced current is then calculated given the simulated electric field of Fig. 3, considering the known drift velocity/electric field relation in GaAs. The total current is the sum of the contribution of all the electrons and holes in the active region.

In simulation of time response, incident light of 850-nm wavelength was used. The generation time is so small that it can be considered instantaneous. The initial electron–hole pairs are exponentially generated along the direction that the light is traveling, as well as uniformly laterally, i.e.,

$$\begin{aligned} n(y) &= n_0 \exp(-\alpha y) \\ n(x) &= \text{const} \end{aligned} \tag{2}$$

where α is the absorption coefficient, and y is the depth.

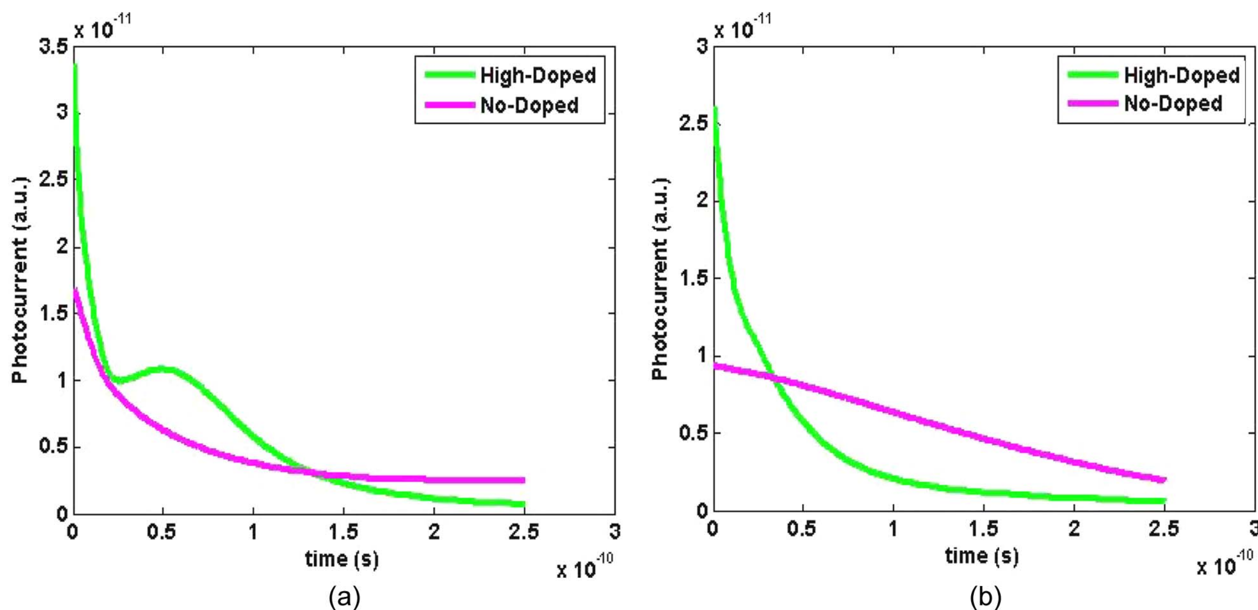

Fig. 7. Time evolution of (a) electrons and (b) holes in the doped and undoped 2DHG devices.

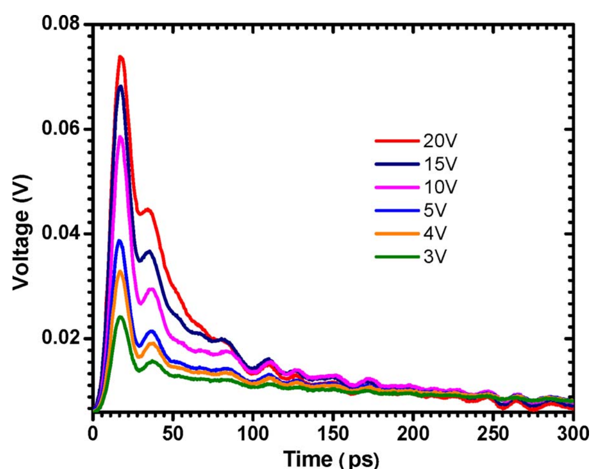

Fig. 8. Time response of the 2DHG devices at different applied biases.

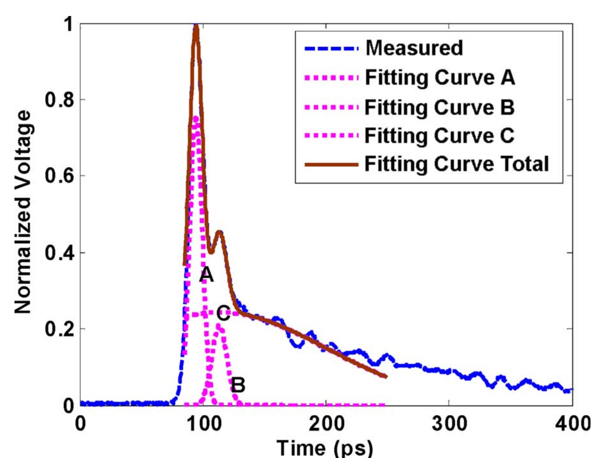

Fig. 9. Decomposition of the time response into three Gaussian components.

C. Dynamic Simulation Results

The time response was simulated by using the ISE-generated 2-D field and calculating the field-dependent drift velocity on a table lookup basis for unintentionally doped GaAs. Photocurrent is then calculated by summing over the contributions from every carrier while it is in motion. After each time step, the charge distributions in the unit cell were recalculated and updated. The corresponding dynamic simulation results for the 2DEG device are shown in Fig. 5, where the total current and its separate electron and hole components are shown. The total time response of the δ-doped structure has a faster initial response but a long tail. Detailed investigation reveals that the fast initial stage is due to electrons, whereas the long tails are due to holes, as expected. The full-width at half-maxima (FWHMs) of intrinsic response are 8.2 and 2.4 ps, respectively, for the undoped and δ-doped structures, which take the saturation velocity into account. The comparison between the doped and undoped structure shows an enhanced electron transport due to the vertical field in the doped structure, although the hole transit time is extended. Furthermore, the time response of the 2DEG device remains independent of the distance between the cathode and the anode, as the carrier motion is vertical to the 2-D reservoir. This has previously been experimentally reported [12].

Simulation results of the doped 2DHG devices are shown in Fig. 6. Each time step shows the state of each of the carrier types and their contribution to the total current. The figure traces the evolution of the electron and hole concentrations in the active region and the corresponding time-resolved response.

TABLE I
PARAMETERS FOR CURVE FITTING OF TIME RESPONSE WITH GAUSSIAN DISTRIBUTIONS FOR DIFFERENT BIAS CONDITIONS

Voltage (V)	σA(ps)	σB(ps)	σC(ps)
20	5.1	8.0	45
15	5.1	7.0	70
10	5.0	6.1	80
5	4.8	5.6	95
4	4.8	5.6	110
3	4.8	5.6	120

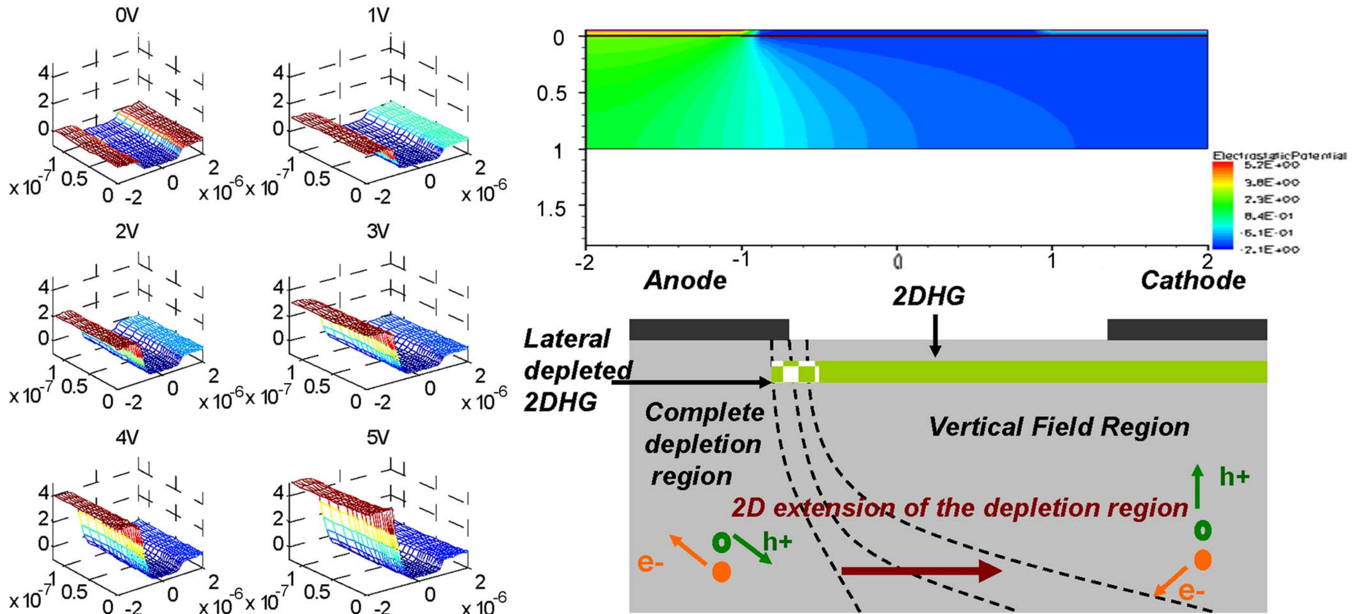

Fig. 10. Left: Electrostatic potential landscape as a function of voltage. Top right: Potential distribution under a 5-V bias. Bottom right: Different parts of the potential landscape.

Fig. 7 separately compares the total time response of the doped and undoped 2DHG devices for electrons and holes. The hole component shown in Fig. 7(b) shows that the doped device has an abbreviated tail due to fast collection of holes. The electron component of the current, however, contains two peaks and experiences a longer transit time in the doped device, consistent with the vertical field driven by the 2DHG, which facilitates the hole transport at the expense of electron transit.

IV. Experimental Evaluation

High-speed time-response measurements were conducted using a mode-locked Ti:sapphire laser, operating at a repetition rate of 76 MHz that generated 150-fs optical pulses over a wavelength tuning range of 720–980 nm. A Tektronix 11801C 50-GHz oscilloscope with an SD-32 sampling head was used, along with a 50-GHz bias-T.

The 2DEG device presents a high-speed response. To understand the influence of the vertical field, time responses for finger gaps of 2- and 4-μm devices are characterized. The FWHM for a 2-μm device is 7.74 ps, and that for a 4-μm device is 8.15 ps, corresponding to cutoff frequencies of 33 and 31.7 GHz, respectively [21]. We observe that the FWHM for the finger gap of a 4-μm device is close to that of a 2-μm device, which is consistent with the expectation borne out by simulations that the drift of electrons between the cathode and the anode is not limiting the device response. For conventional MSM PDs, the empirical formula FWHM $= L_g/1.06 \times 10^7 + 0.26$ ps predicts the FWHM for a 4-μm device to be about 42% larger than that for a 2-μm device for a conventional MSM structure. However, here, we observe a difference of around 5% when the finger separation is doubled [22], [23].

The time response of the 2DHG device at various applied biases is shown in Fig. 8. The existence of 2DHG has been manifested by the capacitance–voltage relationship [24]. The device is much slower than its 2DEG counterpart, as expected, since this device is designed to elicit the dynamics of the slow carriers; it facilitates hole collection while hampering electron motion. The time response does not consist of single time constants either, and, consistent with simulation results of Fig. 7(a), signifies separate transport processes.

The time response can be decomposed into three Gaussian components, as shown in Fig. 9, when a bias of 15 V is applied. All the time responses of Fig. 8 can similarly be decomposed, as shown in Table I, as a function of the standard deviation σ.

Each of these Gaussian components suggests different carrier dynamics. Curves A and B are independent of the voltage, whereas C exhibits obvious voltage dependence. Analysis of the time response requires a closer inspection of the potential landscape that determines carrier velocity, as shown in Fig. 10. Three areas are differentiated on the bottom right of the figure on the basis of the simulation data on the top right. These include a high-field depletion region under the anode pointing downward, a high-field region under cathode pointing upward and due to the 2DHG, and a third region of a relatively low field that laterally extends as a function of the applied bias. The first two regions are independent of the applied bias, whereas the third lateral region extends with bias toward the cathode. Holes that are generated in the active region vertically move to the cathode and to the 2DHG. Electrons, on the other hand, are forced downward, into the low-field region, before being collected at the cathode. That is, curves A and B correspond to the vertical motion of electrons and holes in the active region, respectively, whereas curve C is due to the lateral motion of electrons at the bottom of the active region. These observations are, in fact, consistent with the snapshots of carriers simulated in Fig. 6 and the time response calculated in Fig. 7.

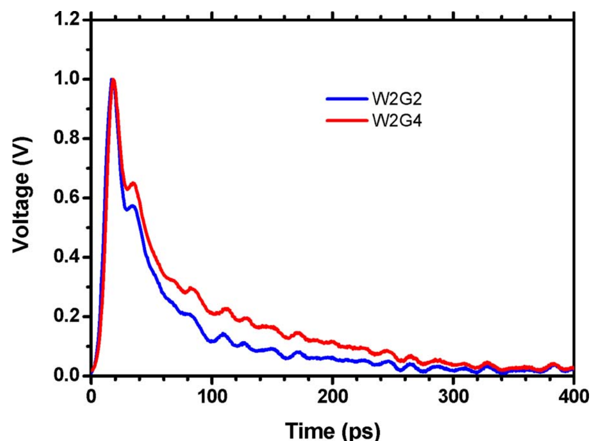

Fig. 11. Comparison of the time responses of the 2DHG devices with 2- and 4-μm finger separations.

TABLE II
PARAMETERS FOR CURVE FITTING OF TIME RESPONSE FOR FINGER SEPARATION OF 2- AND 4-μm DEVICES

Finger Gap (μm)	σA(ps)	σB(ps)	σC(ps)
2	5.1	8.0	45
4	5.0	8.0	68

Further experimental time responses for different geometries verify the aforementioned analysis. Fig. 11 plots the amplitude-normalized time response for devices in which contact separation has been doubled. The external voltage for both devices is 20 V. Table II lists the corresponding standard deviation of the three Gaussian components that constitute the total response. In both devices, the vertical motions of electrons and holes, namely, components A and B in Fig. 9, remain independent of the contact separation, whereas curve C, due to the lateral electron motion at the bottom of the device, is different and distinguishes the two traces. This suggests that the tail of response due to holes can substantially be abbreviated by introducing a 2DHG reservoir of charge and using it to collect the optically generated holes; however, care must be taken to accommodate the electrons so as not to unnecessarily retard electron motion.

Regardless of the slow electron contribution, the doped (2DHG) device shows a shorter tail compared to the undoped device, as shown in Fig. 12. The undoped device has a smaller FWHM, but a crossover of the long tails is observed.

V. Conclusion

We have simulated, fabricated, and characterized 2-D gas, including 2DEG- and 2DHG-based MSM PDs. Static device simulation based on Schrödinger and Poisson's equations was combined with dynamic response formulation based on Ramo's theorem to study the effect of an internal field in the behavior of a heterojunction MSM. For the 2DEG device, we observe that the introduction of δ-doping significantly changes the 2-D field profiles from a laterally oriented field to a vertical one, which affects the trajectory of photogenerated carriers. This greatly modifies the transit time, which is the decisive factor for dynamic response, namely, the speed performance of the PD. Furthermore, the reservoir of charge that is confined to the vicinity

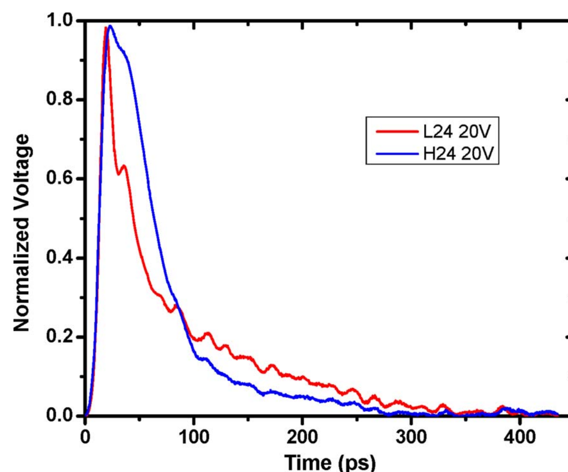

Fig. 12. Normalized time responses of the doped and undoped devices with the same 4-μm finger separation.

of the heterojunction and blocked by Schottky contacts acts as an extended contact, collecting the optically generated carriers.

The 2DEG device showed a fast initial response due to the structure advantage on electron transport, but a long tail due to repulsion of holes. It also verified that the electron component of the total current becomes almost independent of contact separation with a FWHM that changes by less than 5%, even when the spacing between the cathode and the anode doubles.

For the 2DHG device, analysis of the experimental results is more involved due to the more complicated nature of the electrostatic potential profile. We identified three major transport processes in the transient response, two of which are associated with the dynamics due to electron and hole transports when subject to the vertical field in the absorption region. The third process is due to the electrons that have to laterally move at the bottom of the device in a low-field region with speed below saturation velocity. Simulation results verified the experiments and identified these transport mechanisms.

In short, the 2-D gas-based MSM PDs transform the intrinsic field orientations by introducing a δ-doped layer, thus creating a vertical field in the active region. The reservoir of charge facilitates collection of the carriers that reach it without requiring complete transit to the contacts. The separate configuration of the 2-D gas, either 2DEG or 2DHG, enhances one type of carrier transport at the expense of retarding the other. A structure with the combination of 2DEG and 2DHG should be able to compensate the shortcomings of individually using each and provide a potential solution to improve the bandwidth–efficiency product performance by circumventing the need for drift transit of the carriers to the contacts.

References

[1] T. Sugeta and T. Urisu, "WP-B2 high-gain metal–semiconductor–metal photodetectors for high-speed optoelectronic circuits," *IEEE Trans. Electron Devices*, vol. ED-26, no. 11, pp. 1855–1856, Nov. 1979.

[2] J. Harari, J.-P. Vilcot, and D. Decoster, "Metal semiconductor metal photodetectors," in *Wiley Encyclopedia of Electrical and Electronics Engineering*, vol. 12, J. G. Webster, Ed. New York: Wiley, 1999, pp. 561–577.

[3] M. Ito, O. Wada, K. Nakai, and T. Sakurai, "Monolithic integration of a metal–semiconductor–metal photodiode and a GaAs preamplifier," *IEEE Electron Device Lett.*, vol. EDL-5, no. 12, pp. 531–532, Dec. 1984.

[4] K. Kato, “Ultrawide-band/high-frequency photodetectors,” *IEEE Trans. Microw. Theory Tech.*, vol. 47, no. 7, pp. 1265–1281, Jul. 1999.

[5] A. Stõhr, A. Malcoci, A. Sauerwald, I. C. Mayorga, R. Gusten, and D. S. Jager, “Ultra-wide-band traveling-wave photodetectors for photonic local oscillators,” *J. Lightw. Technol.*, vol. 21, no. 12, pp. 3062–3070, Dec. 2003.

[6] K. S. Giboney, M. J. W. Rodwell, and J. E. Bowers, “Traveling-wave photodetector theory,” *IEEE Trans. Microw. Theory Tech.*, vol. 45, no. 8, pp. 1310–1319, Aug. 1997.

[7] K. S. Giboney, R. L. Nagarajan, T. E. Reynolds, S. T. Allen, R. P. Mirin, M. J. W. Rodwell, and J. E. Bowers, “Travelling-wave photodetectors with 172-GHz bandwidth and 76-GHz bandwidth–efficiency product,” *IEEE Photon. Technol. Lett.*, vol. 7, no. 4, pp. 412–414, Apr. 1995.

[8] J.-W. Shi, K.-G. Gan, Y.-J. Chiu, Y.-H. Chen, C.-K. Sun, Y.-J. Yang, and J. E. Bowers, “Metal–semiconductor–metal traveling-wave photodetectors,” *IEEE Photon. Technol. Lett.*, vol. 13, no. 6, pp. 623–625, Jun. 2001.

[9] M. Achouche, V. Magnin, J. Harari, L. Lelarge, E. Derouin, C. Jany, D. Carpentier, F. Blache, and D. Decoster, “High performance evanescent edge coupled waveguide unitraveling-carrier photodiodes for $>$ 40-Gb/s optical receivers,” *IEEE Photon. Technol. Lett.*, vol. 16, no. 2, pp. 584–586, Feb. 2004.

[10] C. Moglestue, J. Rosenzweig, J. Kuhl, M. Klingenstein, M. Lambsdorff, A. Axmann, J. Schneider, and A. Hulsmann, “Picosecond pulse response characteristics of GaAs metal–semiconductor–metal photodetectors,” *J. Appl. Phys.*, vol. 70, no. 4, pp. 2435–2448, Aug. 1991.

[11] M. S. Ünlü and S. Strite, “Resonant cavity enhanced photonic devices,” *J. Appl. Phys.*, vol. 78, no. 2, pp. 607–639, Jul. 1995.

[12] X. Chen, B. Nabet, A. Cola, F. Quaranta, and M. Currie, “An AlGaAs–GaAs-based RCE MSM photodetector with delta modulation doping,” *IEEE Electron Device Lett.*, vol. 24, no. 5, pp. 312–314, May 2003.

[13] W. I. Wang, E. E. Mendez, and F. Stern, “High mobility hole gas and valence-band offset in modulation-doped p-AlGaAs/GaAs heterojunctions,” *Appl. Phys. Lett.*, vol. 45, no. 6, pp. 639–641, Sep. 1984.

[14] S. M. Sze, D. J. Coleman, Jr., and A. Loya, “Current transport in metal–semiconductor–metal (MSM) structures,” *Solid State Electron.*, vol. 14, no. 12, pp. 1209–1218, Dec. 1971.

[15] S. G. Petrosyan and A. Y. Shik, “Contact phenomena in a two-dimensional electron gas,” *Sov. Phys.—Semicond.*, vol. 23, pp. 696–697, 1989.

[16] S. Ramo, “Currents induced by electron motion,” *Proc. IRE*, vol. 27, no. 9, pp. 584–585, Sep. 1939.

[17] E. Sano, “Two-dimensional ensemble Monte Carlo calculation of pulse responses of submicrometer GaAs metal–semiconductor–metal photodetectors,” *IEEE Trans. Electron Devices*, vol. 38, no. 9, pp. 2075–2081, Sep. 1991.

[18] G. B. Tait and B. Nabet, “Current transport modeling in quantum-barrier-enhanced heterodimensional contacts,” *IEEE Trans. Electron Devices*, vol. 50, no. 12, pp. 2573–2578, Dec. 2003.

[19] S. Averin, R. Sachot, J. Hugi, M. de Fays, and M. Ilegems, “Two-dimensional device modeling and analysis of GaInAs metal–semiconductor–metal photodiode structures,” *J. Appl. Phys.*, vol. 80, no. 3, pp. 1553–1558, Aug. 1996.

[20] Z. Susnjar, Z. Djuric, M. Smiljanic, and Z. Lazic, “Numerical calculation of photodetector response time using Ramo’s theorem,” in *Proc. 20th Int. Conf. Microelectron.*, Nis, Serbia, 1995, pp. 717–720.

[21] B. Nabet, A. Cola, A. Cataldo, X. Chen, and F. Quaranta, “Photodetectors based on heterostructures for opto-electronic applications,” *IEEE Trans. Microw. Theory Tech.*, vol. 51, no. 10, pp. 2063–2073, Oct. 2003.

[22] X. Chen, B. Nabet, F. Quaranta, A. Cola, and M. Currie, “Resonant-cavity-enhanced heterostructure metal–semiconductor–metal photodetector,” *Appl. Phys. Lett.*, vol. 80, no. 17, pp. 3222–3224, Apr. 2002.

[23] X. Chen, B. Nabet, X. Zhao, H.-J. Huang, A. Cola, F. Quaranta, A. Taurino, and M. Currie, “Optical and electrical characterization of GaAs-based high-speed and high-sensitivity delta-doped resonant cavity-enhanced HMSM photodetector,” *IEEE Trans. Electron Devices*, vol. 52, no. 4, pp. 454–464, Apr. 2005.

[24] X. Zhao, A. Cola, A. Tersigni, F. Quaranta, E. Gallo, J. Spanier, and B. Nabet, “Optically modulated high-sensitivity heterostructure varactor,” *IEEE Electron Device Lett.*, vol. 27, no. 9, pp. 710–712, Sep. 2006.

Xia (Sarah) Zhao, photograph and biography not available at the time of publication.

Marc Currie, photograph and biography not available at the time of publication.

Adriano Cola, photograph and biography not available at the time of publication.

Fabio Quaranta, photograph and biography not available at the time of publication.

Eric Gallo, photograph and biography not available at the time of publication.

Jonathan E. Spanier, photograph and biography not available at the time of publication.

Bahram Nabet, photograph and biography not available at the time of publication.